Available online at www.sciencedirect.com
SCIENCE DIRECT®
International Journal of Heat and Fluid Flow 25 (2004) 975–985
International Journal of HEAT AND FLUID FLOW
www.elsevier.com/locate/ijhff

Simulations for gas flows in microgeometries using the direct simulation Monte Carlo method

Moran Wang [1], Zhixin Li *

Department of Engineering Mechanics, Tsinghua University, Beijing 100084, People's Republic of China

Received 11 April 2003; accepted 13 February 2004
Available online 20 May 2004

Abstract

Micro gas flows are often encountered in MEMS devices and classical CFD could not accurately predict the flow and thermal behavior due to the high Knudsen number. Therefore, the gas flow in microgeometries was investigated using the direct simulation Monte Carlo (DSMC) method. New treatments for boundary conditions are verified by simulations of micro-Poiseuille flow, compared with the previous boundary treatments, and slip analytical solutions of the continuum theory. The orifice flow and the corner flow in microchannels are simulated using the modified DSMC codes. The predictions were compared with existing experimental phenomena as well as predictions using continuum theory. The results showed that the channel geometry significantly affects the microgas flow. In the orifice flow, the flow separation occurred at very small Reynolds numbers. In the corner flow, no flow separation occurred even with a high driving pressure. The DSMC results agreed well with existing experimental information.
© 2004 Elsevier Inc. All rights reserved.

Keywords: Gas flow; MEMS; Microchannel; DSMC; Orifice flow; Corner flow

1. Introduction

MEMS is an emerging technology with significant potential for future growth. Microsystems based-on MEMS are capable of sensing and controlling physical processes with length scales on the order of one micron, or even sub-micron (Ho and Tai, 1998). Despite the growing number of realized applications of MEMS in scientific and engineering devices, there is only a minimum level of understanding of the fluid dynamics and heat transfer processes in fluidic MEMS (Mohamed, 1999). Performance of MEMS often defies predictions made using scaling laws developed for large systems. As the functions of future MEMS expand, there is a pressing need for reliable computational capabilities for the thermal and fluid dynamic processes in MEMS (Wang and Li, 2002a,b).

In most microflows, the mean free path of the fluid, λ, is of the same order as the system characteristic length, l. So the Knudsen number, which is the ratio of the two lengths, can be quite high even when the fluid is dense. Therefore the continuum assumption breaks down and the flow should be described using a molecular point of view since traditional CFD techniques applied to microflow analyses may lead to large errors. The DSMC method, proposed by Bird (1976, 1994), can successfully simulate gas flows at high Knudsen numbers, and has been widely applied in predictions of supersonic rarefied gas flows (Oran et al., 1998; Bird, 1998). In recent years, the DSMC method has also been used to predict the high-speed gas flow and heat transfer in short straight microchannels (Liou and Fang, 2001; Hadjiconstantinou and Simek, 2002).

In traditional DSMC simulations for supersonic flows, the Dirichlet type of velocity boundary conditions was generally used. This approach is often applied in external flow simulations, which require the downstream boundary to be far away from the base region. However, the flows in microsystems are often subsonic flows, and the boundary conditions which can be obtained from the experiments are always pressure and temperature,

* Corresponding author. Tel.: +86-10-62772919; fax: +86-10-62781610.
E-mail addresses: moralwang99@mails.tsinghua.edu.cn (M. Wang), lizhx@tsinghua.edu.cn (Z. Li).
[1] Tel.: +86-10-62772920.

0142-727X/$ - see front matter © 2004 Elsevier Inc. All rights reserved.
doi:10.1016/j.ijheatfluidflow.2004.02.024

Nomenclature

a	local sound speed (m/s)
A	inlet/outlet cross-sectional area (m^2)
c'	molecular thermal speed (m/s)
C_{mp}	local most probable thermal speed of molecules (m/s)
F	number flux (m^{-2})
k	Boltzmann constant (J/K)
Kn	Knudsen number
m	molecular mass (kg)
n	number density (m^{-3})
N	total number of molecules in a cell
p	pressure (Pa)
Pr	Prandtl number
R	universal gas constant (J/mol K)
R_f	random fraction number
s	molecular speed ratio defined as $s = U\beta$ or $s = V\beta$
T	gas temperature (K)
T_{tr}	translational temperature (K)
T_{rot}	rotational temperature (K)
u, v	molecular velocity components (m/s)
U, V	local streamwise mean velocity components (m/s)

Greeks

β	defined as $1/\sqrt{2RT}$, related to the thermal scattering
δt	time step (s)
ζ	number of rotational degrees of freedom
γ	specific heat ratio
μ	dynamic viscosity (kg/m s)
ρ	density (kg/m^3)
σ_T	heat accommodation coefficient
σ_v	momentum accommodation coefficient

Subscripts

c	centerline properties
e	exit boundary
g	surface gas properties
in	inlet boundary
j	cell position
rot	rotational
s	slip properties
tr	translational
v	momentum
w	surface properties

instead of velocity and number density. Although these issues are well known, methods to impose effectively boundary conditions for DSMC for microgas flow simulations have not been as widely studied as those for continuum CFD. Piekos and Breuer (1996) introduced a particle-based method on the differences between a targeted number density and the values calculated by the ideal gas relations. Ikegawa and Kobayashi (1990) and Nance et al. (1998) applied characteristic-based boundary conditions at the downstream boundary and the number flux to determine the velocity at the upstream boundary. Wu and Tseng (2001) and Wu et al. (2001) developed the particle-based method and applied it at both the upstream and downstream boundaries. The particle-based implements of pressure boundary condition for low-speed flows have a disadvantage that the simulation may be unstable due to the low particle flux (Cai et al., 2000). To overcome this disadvantage, Liou and Fang (2000) developed a local-cell-averaged method to calculate the inlet mean velocity. The method was very simple and could be proved to be consistent with Nance's approach. However, the local-cell-averaged velocity did not embody the pressure effect at the upstream boundary. Therefore, the astringency is inefficient. In the present paper, a new implicit treatment for the upstream boundary condition is proposed and theoretically analyzed for the DSMC of low-speed microflows. The new implement of boundary conditions does not only overcome the instability of particle-based approaches, but also has a faster astringency than Liou's method. Additionally, in most of DSMC simulations for microflows, both the downstream and the upstream flows have a same direction. However, many contrary cases occur in practice, to which very little attention has been paid yet. Wu and Tseng (2001) simulated flows in a T-shape micromanifold, however, with little detail descriptions of the boundary implements. In this paper, the formulations for boundary conditions are derived theoretically when the upstream and downstream flow directions are not consistent.

Especially, the current paper is mainly concerned with the gas flow behavior in microgeometries such as channels with an orifice or a bend, since these kinds of microdevices are often encountered in microsystems. Experimental results (Li et al., 2000) showed a larger pressure loss than predicted by classical laminar flow theory in such microchannels. Lee et al. (2001a,b) suggested that flow separation may have led to the unusual pressure drops. In this study the DSMC method with new boundary treatments was employed to predict the flow behavior in microgeometries. The results were compared with the existing experimental data and simulations based on the continuum assumption.

2. Numerical method

DSMC is a molecular-based statistical simulation method for rarefied gas flow introduced by Bird (1976, 1994). The method numerically solves the dynamic equations for gas flow using thousands of simulated molecules. Each simulated molecule represents a large number of real molecules. With the assumption of molecular chaos and a rarefied gas, only the binary collisions are considered, so the molecular motion and their collisions are uncoupled if the computational time step is smaller than the physical collision time. The interactions with boundaries and with other molecules conserve both momentum and energy. The macroscopic flow characteristics are obtained statistically by sampling the molecular properties in each cell. At the beginning of the calculation, the simulated particles are uniformly distributed statistically in the cells. At each time step, all particles move according to their individual velocities, interact with the boundaries and then are indexed. In each cell, a certain number of collision pairs are selected using the no-time-counter (NTC) method and collisions are calculated. These steps are repeated until the statistical errors are small enough. The DSMC method can simulate non-equilibrium and unsteady gas flow. A steady-state flow field is obtained with a sufficiently long simulation time. The present simulations used the variable hard sphere (VHS) model (Bird, 1994). The time step was selected so that each simulated molecule would move a 0.2-cell-size displacement at the most probable molecular speed.

2.1. Pressure boundary conditions

As referred above, in traditional DSMC simulations, which have been widely applied to supersonic external flows, the boundary conditions are always the number density and the freestream velocity. However in low-speed microflows, this data is hard to obtain from experiments. Therefore, the DSMC boundary conditions should be pressure boundaries instead of density boundaries. Generally, the inlet pressure and temperature, P_{in} and T_{in}, and the outlet pressure, P_{e}, are known from experiments, and these three parameters will determine the flow.

2.1.1. Upstream pressure conditions

Various upstream pressure boundaries have been proposed for subsonic gas flow. Ikegawa and Kobayashi (1990), Nance et al. (1998), Wu and Tseng (2001) and Wu et al. (2001) determined the mean flow velocity at the inlet by the number flux within a time step,

$$(u_{\text{in}})_j = \frac{(\dot{n}_+ - \dot{n}_-)_j}{n_j A} \tag{1}$$

where the subscripts + and − refer to particle fluxes in the positive and negative flow directions, respectively, n is the number density and A the boundary cross-sectional area. $\dot{n}$ is the number flux determined by averaging over the whole inlet boundary.

$$\dot{n} = \frac{n}{2\sqrt{\pi}\beta}\left[\exp(-s^2\cos^2\theta) + \sqrt{\pi}s\cos\theta\{1+\operatorname{erf}(s\cos\theta)\}\right] \tag{2}$$

where 'erf' represents the error function, and the value of θ is the angle between the velocity vector and normal to the boundary element. Ikegawa and Kobayashi (1990) used the particle-conservation concept to come up with a constant inflow velocity, and determined the particle fluxes by actually counting the number of particles crossing the computational boundary. In contrast, Nance et al. (1998) and Wu and Tseng (2001) and Wu et al. (2001) applied the particle conservation on a per-cell basis, and determined the velocity components of the entering particle using the acceptance–rejection method and the Maxwellian distribution function.

However, in both methods, (nA) and $(\dot{n}_+ - \dot{n}_-)$ are both small numbers for low-speed flows within a single time step. Therefore the scattering may be rather large, which causes the numerical solution to be unstable. Additional effort is needed to reduce the scattering. Fang and Liou (2002) proposed a simpler treatment for the inlet boundary using a first-order extrapolation to determine the inlet mean velocity from inside the computational domain.

$$(u_{\text{in}})_j = u_j \tag{3}$$

This method is easy to use, and it can be proved consistent with Nance's method. However, it takes a long time to converge because the velocity of coming particles does not embody the pressure information. It also shows that this treatment has some difficulties when the wall temperature is quite different from the gas temperature. Here we proposed another treatment for the upstream pressure boundary based on the theory of characteristics:

$$(u_{\text{in}})_j = u_j + \frac{p_{\text{in}} - p_j}{\rho_j a_j} \tag{4}$$

$$(v_{\text{in}})_j = v_j \tag{5}$$

The number density is obtained from the equation of state for the given pressure and temperature.

$$n_{\text{in}} = \frac{P_{\text{in}}}{kT_{\text{in}}} \tag{6}$$

The particle number fluxes and the velocity components of entering molecules are determined locally from the Maxwellian distribution.

2.1.2. Downstream pressure conditions

For the downstream boundary, the same treatment is applied. The equations below have also been applied and verified by Nance et al. (1998) and Liou and Fang (2000).

$$(\rho_e)_j = \rho_j + \frac{p_e - p_j}{(a_j)^2} \tag{7}$$

$$(u_e)_j = u_j + \frac{p_j - p_e}{\rho_j a_j} \tag{8}$$

$$(v_e)_j = v_j \tag{9}$$

$$(T_e)_j = P_e \Big/ \left[(\rho_e)_j R\right] \tag{10}$$

Eqs. (7)–(10) describe the downstream pressure conditions for an x-direction outlet. For a y-direction outlet, Eqs. (8) and (9) should be modified as follows:

$$(u_e)_j = u_j \tag{11}$$

$$(v_e)_j = v_j + \frac{p_j - p_e}{\rho_j a_j} \tag{12}$$

The current implementation of the characteristics-based equations ensures proper accounting of the mass influx from the exit boundary and the overall mass balance in the microchannels. The mean quantities are defined as sample average values.

$$u_j = \frac{1}{N_j}\sum u \tag{13}$$

$$v_j = \frac{1}{N_j}\sum v \tag{14}$$

$$\rho_j = n_j m \tag{15}$$

$$T_j = (3T_{tr} + \zeta T_{rot})/(3+\zeta) \tag{16}$$

$$P_j = n_j k T_j \tag{17}$$

The calculated mean quantities are then used in equations to determine the number and the velocity distribution of the molecules entering the computational domain from the exit boundary.

2.2. Implicit velocity treatment

In most previous simulations, gases always flow in one direction, so the velocity distribution is easily treated as description by Bird (1994). However, different cases are often encountered in practice such as gas flows turning a 90° angle. Such examples are referred in a few authors (Wu and Tseng, 2001), but little details of velocity treatment were presented. In this section, the implicit velocity treatment is introduced in detail.

Generally, the gas flow can be treated as quasi-equilibrium, so the quantities associated with the molecules entering the computational domain from either the upstream inlet boundary or the downstream exit boundary can be determined according to the Maxwellian equilibrium distribution function,

$$f_0 = \frac{\beta^3}{\pi^{3/2}} \exp(-\beta^2 c'^2) \tag{18}$$

The Maxwellian distribution function can be used to calculate the number flux of the molecules entering the computational domain based on the local temperature and the mean flow velocity.

At the inlet boundary, the streamwise thermal velocity, u', of the molecules entering the computational domain should be in the interval $[-U_j, \infty]$, with a distribution function,

$$f_{u'} \propto (\beta u' + s_j)\exp(-\beta^2 u'^2) \tag{19}$$

The numerical implementation of the acceptance–rejection method in Eq. (19) replaced the upper limit of ∞ by a cut-off value of $3C_{mp}$, where C_{mp} represents the local most probable thermal speed of the molecules,

$$C_{mp} = \sqrt{2RT_j} \tag{20}$$

Therefore, the thermal velocity, u', is randomly sampled in the interval $[-U_j, 3C_{mp}]$. The resulting streamwise total velocity, $u = U_j + u'$, of the molecules entering the computational domain is then

$$u = (U_{j,in} + 3C_{mp})R_f \tag{21}$$

The two cross-stream velocity components are assumed to be of the following form,

$$v = A\cos\phi + V_{j,in} \tag{22}$$

$$w = A\sin\phi \tag{23}$$

The magnitude, A, lies between 0 and ∞, with a distribution function

$$f_A = \exp(-\beta^2 A^2) \tag{24}$$

Using the acceptance–rejection method, the magnitude, A, can be written as

$$A = \sqrt{-\ln(R_f)}/\beta = \sqrt{-\ln(R_f)}C_{mp} \tag{25}$$

The angle, ϕ, is uniformly distributed between 0 and 2π:

$$\phi = 2\pi R_f \tag{26}$$

Similarly, at the downstream exit boundary, the streamwise thermal velocity of a molecule entering the computational domain from the x-direction downstream is set in the interval $[-3C_{mp}, -U_j]$, while a molecule from y-direction downstream is in the interval of $[-3C_{mp}, -V_j]$. Therefore the resulting velocity component distributions for molecules entering the computational domain are

For an x-direction outlet:

$$u = (U_{j,out} - 3C_{mp})R_f \tag{27}$$

$$v = A\cos\phi + V_{j,\text{out}} \tag{28}$$

$$w = A\sin\phi \tag{29}$$

For a y-direction outlet:

$$u = A\cos\phi + U_{j,\text{out}} \tag{30}$$

$$v = (V_{j,\text{out}} - 3C_{\text{mp}})R_{\text{f}} \tag{31}$$

$$w = A\sin\phi \tag{32}$$

3. Verifications

The new implicit boundary treatment was implemented into the DSMC code originally developed by Bird (1994). The modified DSMC code was used to simulate a micro-Poiseuille flow as shown in Fig. 1. The channels were 5 μm×1 μm with 50×50 uniform rectangular cells and 4×4 sub-cells in each cell. First, the computational results were compared with analytical results based on the Navier–Stokes equations with slip boundary conditions. Then, the present method was also compared with other boundary treatments in astringency.

For pressure-driven micro-Poiseuille flow, the velocity is a function of local Knudsen number (defined by local density in each cell) and the distance to the wall as well as the pressure gradient. For a fully diffuse reflecting wall where $\sigma_v = 1$, the dimensionless velocity normalized by the centerline value are (Beskok, 1996)

$$\frac{u}{u_{\text{c}}} = \left[-\left(\frac{y}{h}\right)^2 + \frac{y}{h} + Kn \right] \Big/ \left(\frac{1}{4} + Kn\right) \tag{33}$$

$$\frac{u}{u_{\text{c}}} = \left[-\left(\frac{y}{h}\right)^2 + \frac{y}{h} + \frac{Kn}{1+Kn} \right] \Big/ \left(\frac{1}{4} + \frac{Kn}{1+Kn}\right) \tag{34}$$

With Eqs. (33) and (34), the slip velocity distribution along the wall for the first-order and high-order approximations can be written as

$$\frac{u_{\text{s}}}{u_{\text{c}}} = Kn \Big/ \left(\frac{1}{4} + Kn\right) \tag{35}$$

$$\frac{u_{\text{s}}}{u_{\text{c}}} = \frac{Kn}{1+Kn} \Big/ \left(\frac{1}{4} + \frac{Kn}{1+Kn}\right) \tag{36}$$

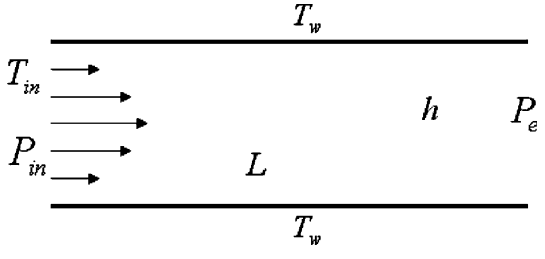

Fig. 1. Sketch of micro-Poiseuille flow.

where Kn is the local Knudsen number on the wall which varies as the flow develops downstream.

Three cases were analyzed numerically to verify the implementation of the boundary conditions for the micro-Poiseuille flow. The inlet and outlet pressures for case 1 were 1.5×10^5 and 0.5×10^5 Pa, for case 2 they were 0.6×10^5 and 0.15×10^5 Pa and for case 3 they were 0.2×10^5 and 0.04×10^5 Pa. Both the wall and the oncoming gas temperatures were 300 K. The dimensionless velocity profiles at about 2/3 channel length from the inlet for the three cases are shown in Fig. 2. The local Knudsen numbers labeled in the figures are 0.0386, 0.1785 and 0.5371, which are defined by the local averaged gas densities. For the small Knudsen number cases, the DSMC results agree well with both the first-order and the second-order analytical calculations. For the large Knudsen number case, the DSMC method and the second-order approximation agree well, while the first-order profile diverges from the DSMC results as Kn increases, with the largest difference occurring at the channel wall.

The normalized slip velocity distributions for the first-order and second-order analyses are compared with the present DSMC predictions in Fig. 3 for cases 1 and 3. In case 1, the Knudsen numbers are small, from 0.0358 to 0.0958, so the three curves agree very well. As the Knudsen number increased, the first-order distribution separates from the other curves. In case 3, the Knudsen numbers were high, from 0.268 to 1.077. The first-order approximation is no longer valid for this case and predicts a much higher slip velocity distribution than the other two methods.

The present boundary treatment is also compared with previous ones. Since Liou's method has shown a better efficiency than other methods (Liou and Fang, 2000), this paper compares the present method to Liou's in accuracy and astringency. Fig. 4 shows the pressure along the channel centerlines resulted from the two boundary treatments for case 1. The results are also compared with the Arkilic's slip and non-slip formulations (Arkilic, 1997) and the NS based simulation results (performed by FLUENT 6.0). The pressure distributions from the present method and Liou's method are consistent completely, which indicates the accuracy of the present method. The evolutions of normalized pressure at inlet and outlet are shown in Fig. 5(a) and (b). The results of only early 6000 sample sizes are compared between the two methods. It is clear that the present method has a better astringency than Liou's method. Therefore, the results showed that the proposed implicit treatments of the boundary conditions are robust and appropriate for microflow predictions.

In Fig. 4, the DSMC methods are compared with continuum based methods. The pressures resulted from the latter agree with those from the former, however,

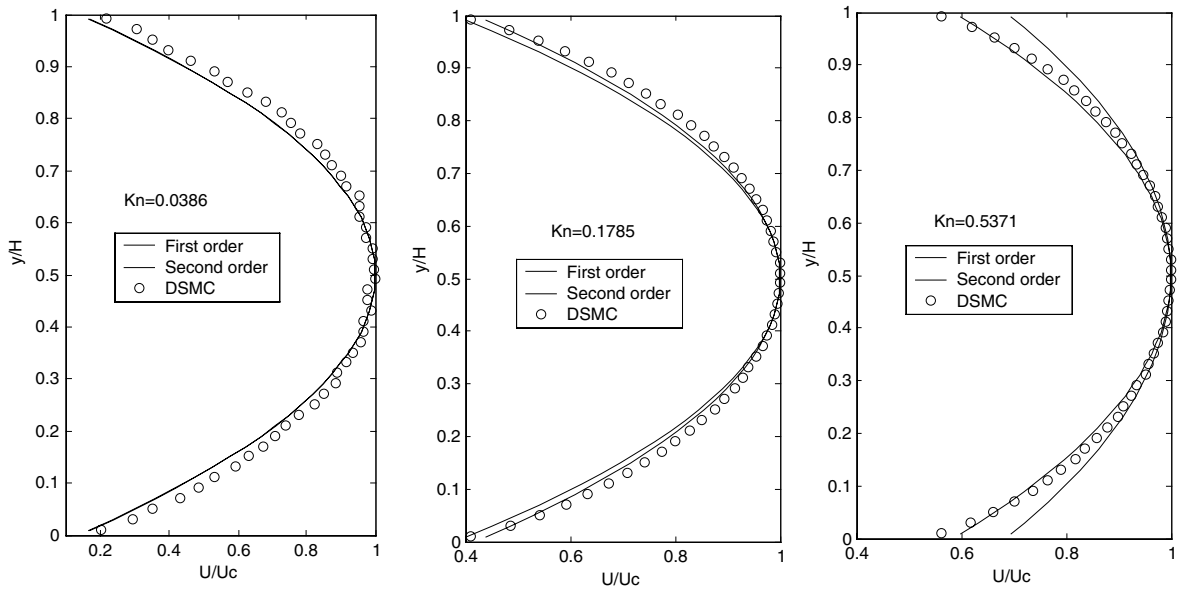

Fig. 2. Comparison of velocity profile for micro-Poiseuille flow at different Knudsen numbers.

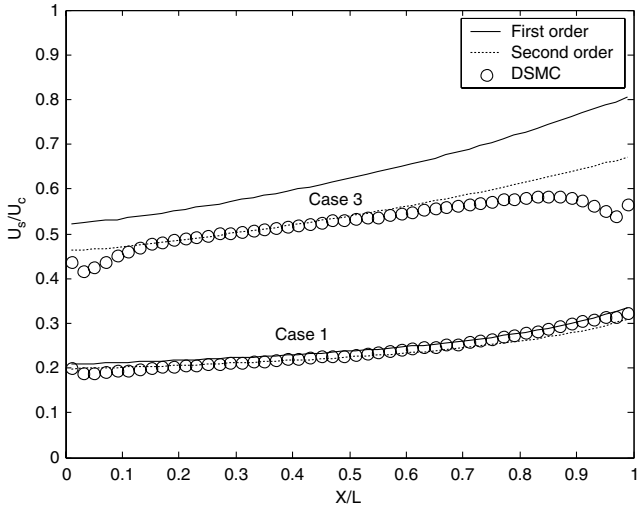

Fig. 3. Comparison of normalized slip velocity distributions for micro-Poiseuille flow for $Kn = 0.027$–0.051 (case 1), and $Kn = 0.268$–1.077 (case 3).

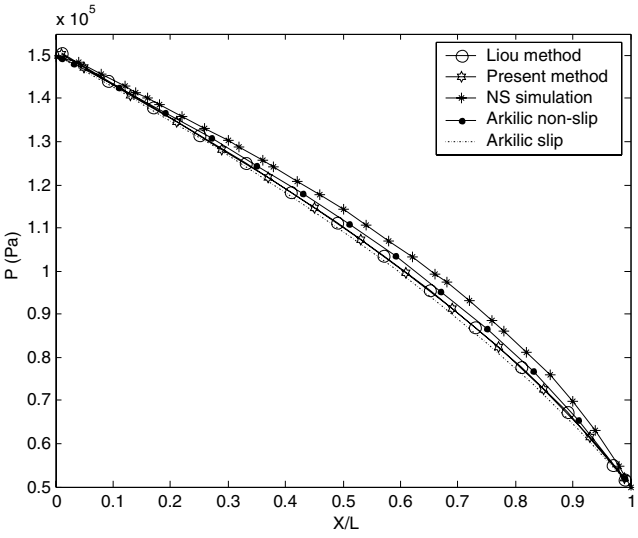

Fig. 4. Pressure along the centerline of microchannels from different boundary treatments.

with a little departure in details. The differences in pressure distributions lead to different mass flow rates. Both the DSMC methods resulted in 1.27×10^{-4} kg/s mass flow rate. The value of Arkilic's slip formulation is 1.39×10^{-4} kg/s, and that of Arkilic's non-slip formulation is 1.05×10^{-4} kg/s. The NS based simulation performed by the commercial code in a non-slip model obtained a value at 1.01×10^{-4} kg/s. These results show that though the pressure distributions resulted from the particle and continuum based methods are very close, the mass flow rate can be different over 10% for an outlet Knudsen number at near 10^{-1}.

4. Results and discussions

The flow in two types of microgeometries was investigated using the two-dimensional DSMC codes with the modified implicit boundary condition treatments. The first geometry was a straight microchannel with a rectangular orifice, while the second geometry was a bended microchannel with a rectangular corner. The flows in these two types of channels were experimentally investigated by Li et al. (2000) and Lee et al. (2001a,b), so the simulations were compared with their experimental results.

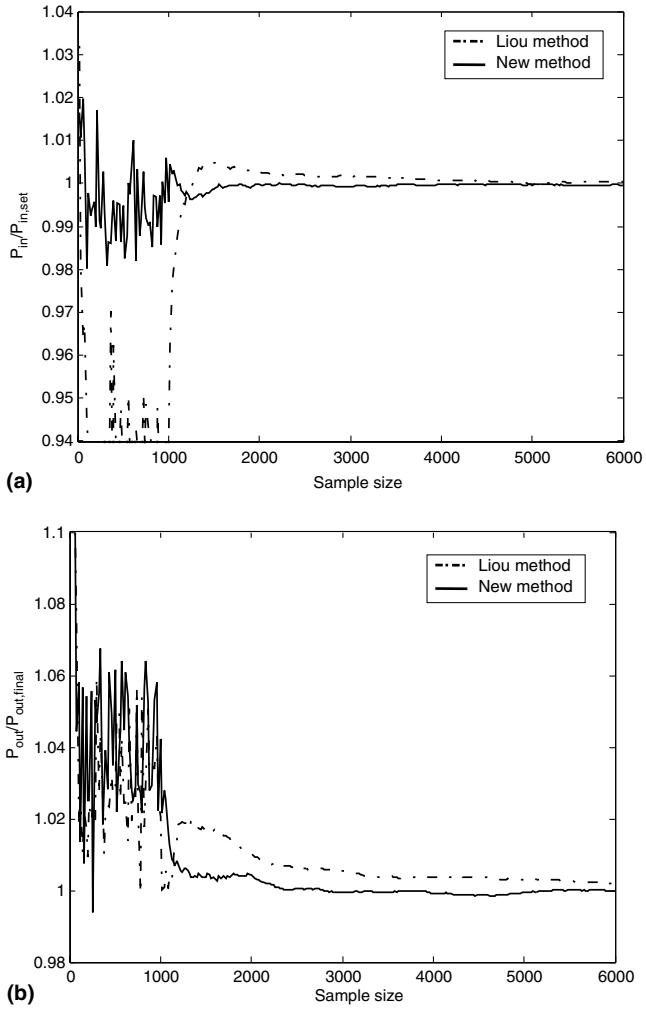

Fig. 5. Evolution of averaged pressure at the inlet from different methods. (a) Normalized inlet pressure and (b) normalized outlet pressure.

4.1. Orifice flow

Gas flow in a straight microchannel with an orifice is often encountered in microsystems. The basic structure of the orifice flow channel is shown in Fig. 6. The channel has a length L and a height H. The rectangular orifice at the center of the channel has a width d and a length l. The inlet pressure and temperature and the outlet pressure are given. The properties of the nitrogen gas were taken from Bird (1994). In the simulations, the channel length L was 20 μm, the height H was 4 μm and

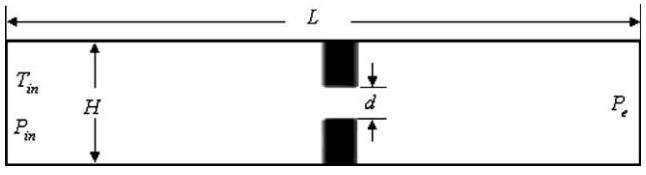

Fig. 6. Basic structure and boundary conditions for the orifice flow.

Table 1
Orifice flow parameters

Case	P_{in} ($\times 10^5$ Pa)	n_∞ ($\times 10^{25}$)	N_{total}	N_{sample}
1	1.5	3.6216	155,912	865,050
2	2.0	4.8287	140,475	724,050
3	2.5	6.0359	130,977	596,050
4	3.0	7.2431	124,942	520,050

both the orifice width d and the orifice length l were 1 μm. The inlet temperature T_{in} was 300 K and the outlet pressure P_e was 1×10^5 Pa. The inlet pressure P_{in} ranged from 2×10^5 to 3×10^5 Pa. The four cases are listed in Table 1, where N_{total} represents the total number of simulated particles and N_{sample} is the sample number. The variable hard sphere (VHS) model was used. 200×40 uniform rectangular cells with 4×4 sub-cells in each cell were applied to ensure the sub-cell size is smaller than the local mean free path in the simulations (Alexander et al., 1998). Over 1×10^5 molecules were simulated and the sample sizes were over 5×10^5. Convergence was also verified by monitoring mass balance; maximum errors were less than 0.3%.

Like all constriction–expansion devices, the x-velocity continues to increase behind the orifice and then it decreases. The x-velocity distributions along the channel midline are compared in Fig. 7 for different inlet pressures. Larger pressure drops resulted in larger velocities behind the orifice. Fig. 8 shows the temperature distributions along the channel midline for the different inlet pressures. Because the gas is accelerated by the constriction, part of the internal energy is converted to kinetic energy, so the temperature decreases at the orifice. The larger pressure drops then caused lower temperatures behind the orifice.

The averaged pressure distributions along the channel for the different inlet pressures in Fig. 9 show that the

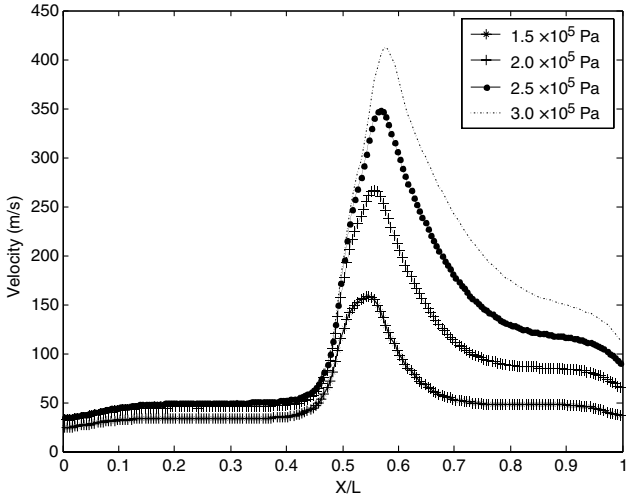

Fig. 7. Velocity distribution of the orifice flow along the channel midline for different inlet pressures.

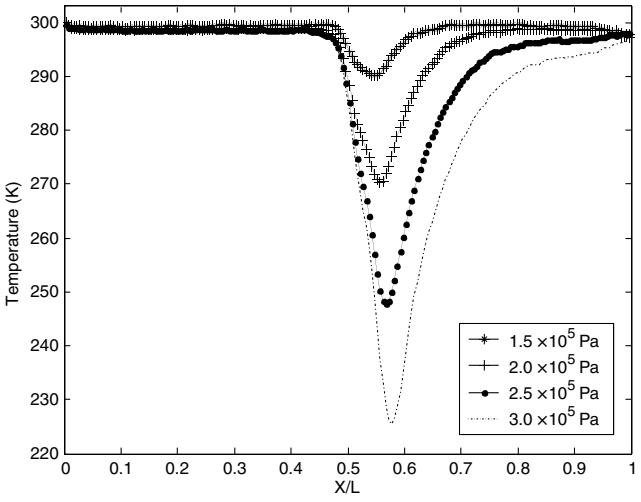

Fig. 8. Temperature distribution along channel midline of the orifice flow for different inlet pressures.

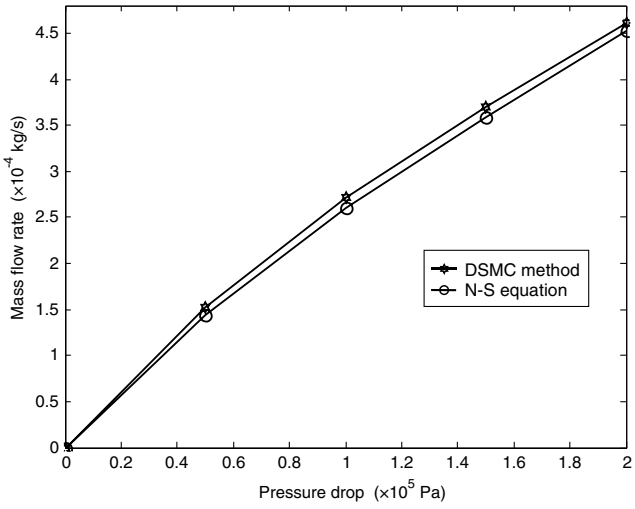

Fig. 10. Mass flow rates for the orifice flow for different pressure drops compared with results based on the no-slip N–S equations with the same pressure boundary conditions.

pressure drop is mainly at the orifice. The pressure is averaged across the channel arithmetically. Before and far behind the orifice, the pressure drop is small and linear. This phenomenon agrees well with experiments (Fig. 5 in Lee et al., 2001a). At the orifice, the pressure decreases sharply, but the decrease is linear. For the larger pressure drops, the pressure behind the orifice is even lower than the exit pressure.

The mass flow rates for the different pressure drops are compared in Fig. 10 with results based on the no-slip compressible Navier–Stokes equations calculated using the commercial code FLUENT 6.0. The mass flow rates from the DSMC prediction are a little larger than those of the no-slip N–S equations. The difference is most likely due to the velocity slip on the wall surfaces. Additional investigation shows that the mass flow rates of orifice flow are less than 1/4 flow rate of straight channel flow with a same flow domain. That indicates the large effect of geometry on the flow behavior.

The detailed flow structure for the orifice flow is given by the streamlines for an inlet pressure at 1.5×10^5 Pa in Fig. 11. The maximum Reynolds number along the channel is less than 10. The streamlines show that separation occurs behind the orifice, which was proved by a resent experiment of Lee et al. (2001b).

4.2. Corner flow

Another case of flow in P_e microchannels with complex geometries often encountered in MEMS is gas flow in bended microchannels. In the present paper, the microchannel flow was analyzed for flow around a rectangular corner. The basic geometry and boundary conditions are shown in Fig. 12. Each leg of the channel is L long and H high. The exit pressure P_e was 1×10^5 Pa. The inlet temperature T_{in} was 300 K. The inlet pressure P_{in} ranged from 2.0×10^5 to 3.0×10^5 Pa. The parameters for the five cases are listed in Table 2. For all the simulations 100×100 uniform rectangular cells (3×3 subcells in each cell) are used with $L = 5$ μm and $H = 1$ μm.

Fig. 13 shows the averaged temperature distributions along the channel for the different inlet pressures. The temperature was the bulk temperature averaged across

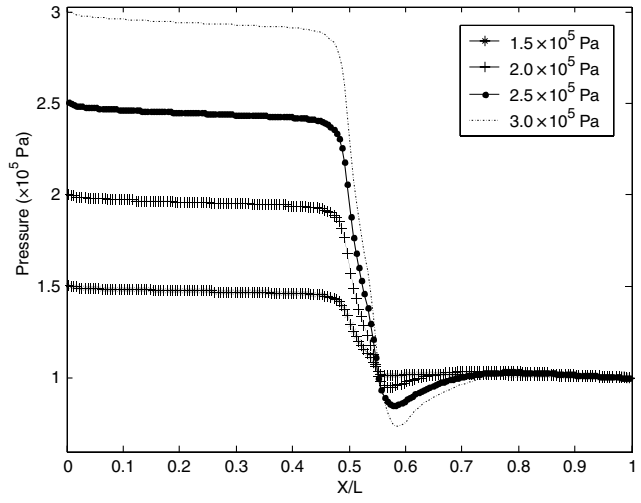

Fig. 9. Averaged pressure distribution along the orifice flow channel for different inlet pressures.

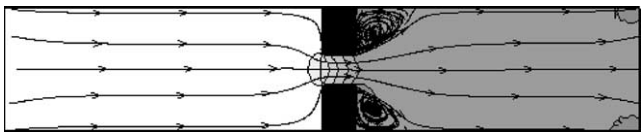

Fig. 11. Streamlines together and pressure contours for the 1.5×10^5 Pa inlet pressure.

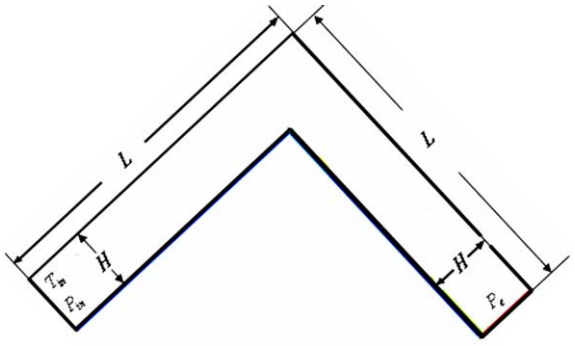

Fig. 12. Basic geometry and boundary conditions for the corner flow.

Table 2
Corner flow parameters

Case	P_{in} ($\times 10^5$ Pa)	n_∞ ($\times 10^{25}$)	N_{total}	N_{sample}
1	2.00	4.8287	166,980	1,000,000
2	2.25	5.4323	163,450	1,000,000
3	2.50	6.0359	159,966	1,000,000
4	2.75	6.6395	157,509	1,000,000
5	3.00	7.2431	156,418	1,000,000

the channel. The x-axis denotes the normalized position along the channel centerline with the corner located at $\frac{x}{2(L-H/2)} = 0.5$. The temperature variation along the channel is similar to that along a straight channel, except for the peak at the corner. The Mach number distributions along the channel for different inlet pressures are compared in Fig. 14. The distribution is similar to two individual pressure-driven straight channel flows. At the corner, the flow is very slow, so the Mach number is even lower than that at the inlet. Fig. 15 shows the pressure distributions along the channel with the pressure averaged over the cross-section at each position. The pressure increased at the corner, while before and after the corner, the pressure distribution is nearly but not exactly linear. This also agrees well with the experimental results (Fig. 3 in Lee et al., 2001b).

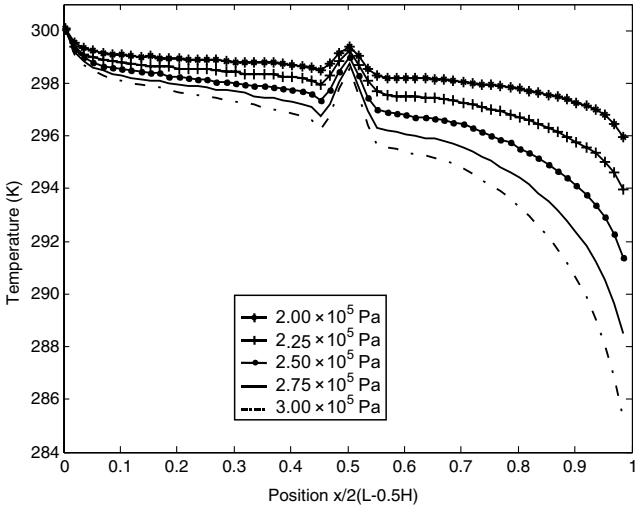

Fig. 13. Averaged bulk temperature distributions along the corner flow channel for different inlet pressures.

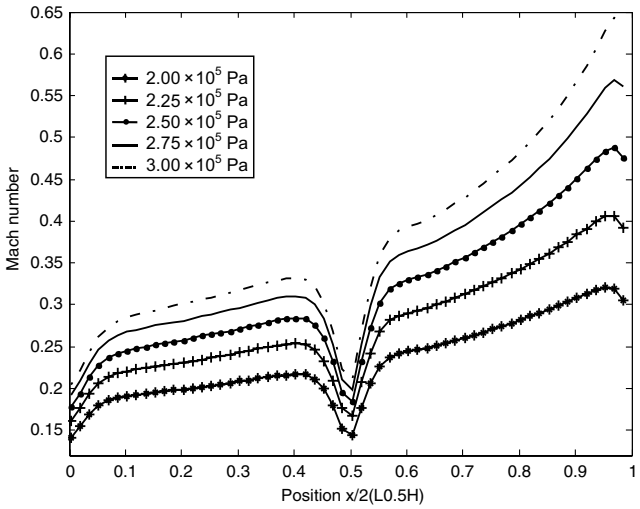

Fig. 14. Mach number distributions along the channel centerline of corner flow for different inlet pressures.

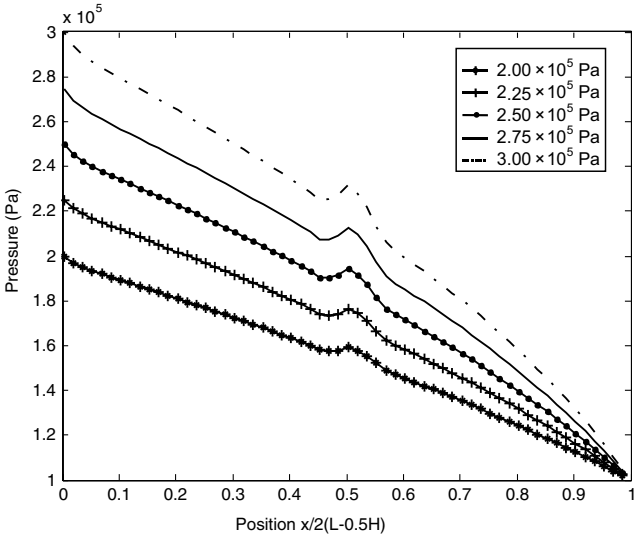

Fig. 15. Averaged pressure distributions along the corner flow channel for different inlet pressures.

The mass flow rates are compared with the results based on the no-slip N–S equation with the same boundary conditions in Fig. 16. Here, the mass flow rate predicted by the DSMC is much larger than predicted by the N–S equations, which implies that the flow in the bended channel is quite different from that in a straight channel. Lee et al. (2001a) ascribed the larger pressure loss in the bended microchannel to the flow separation at the corner. However, the detailed flow structure

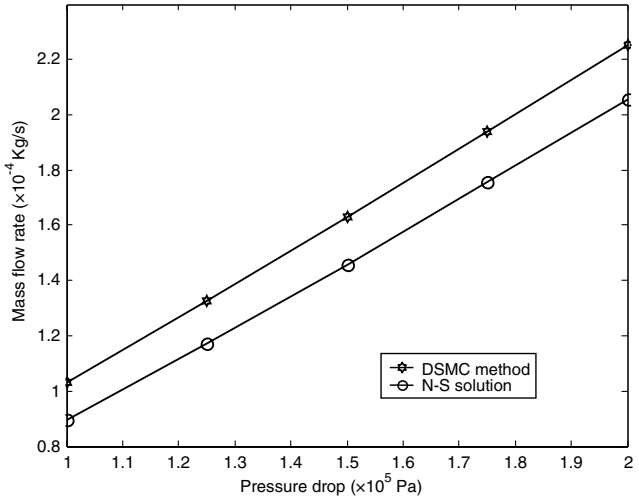

Fig. 16. Mass flow rates for the corner flow channel for different pressure drops compared with results based on no-slip N–S equations with the same pressure conditions.

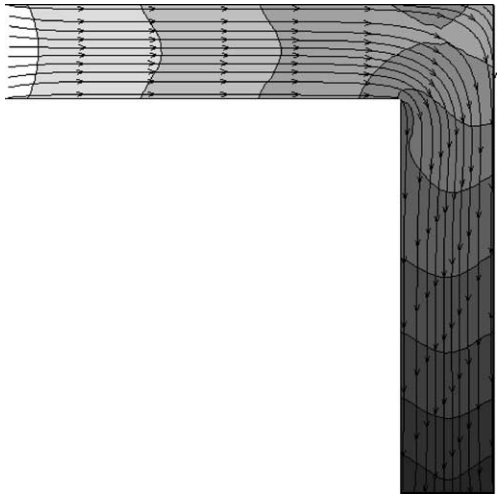

Fig. 17. Streamlines together with density contours for the 3.0×10^5 Pa inlet pressure condition.

shown in Fig. 17 indicates that no flow separation occurs at the corner. Therefore, the larger pressure loss in the bended channel may be related to their aspects of microgas flows.

5. Concluding remarks

New implicit treatments of the boundary conditions for the DSMC method was developed to predict flow in MEMS microchannels. The modified DSMC codes were then used to predict the gas flow behavior in microchannels, including orifice flow and corner flow. The predictions show that the channel geometry, as well as the Knudsen number, significantly affects the fluid dynamics and the thermodynamic behavior in the microchannel flows. In the microorifice flow, the flow separation occurred behind the orifice at very low Reynolds number, but the flow rates were larger than the no-slip continuum theory predictions. In the microcorner flow, no flow separation occurred even for the high flow rate, and the flow rates were much larger than those based on the continuum assumption. The simulation results agree with existing experimental results.

Since gas flows in microgeometries are often encountered in microsystems, the present simulations can provide significant insight for the design of MEMS.

Acknowledgements

The present work was supported by the National Natural Science Foundation of China (grant no. 59995550-2) and the National Key Basic Research and Development Program of China (grant no. 1999033106).

References

Alexander, F.J, Garcia, A.L., Alder, B.J., 1998. Cell size dependence of transport coefficients in stochastic particle algorithm. Phys. Fluids 10, 1540–1542.

Arkilic, E.B., 1997. Measurement of the mass flow and tangential momentum accommodation coefficient in silicon micromachined channels. Ph.D. Dissertation, MIT, Cambridge, MA.

Beskok, A., 1996. Simulations and models for gas flows in microgeometries. Ph.D. Dissertation, Prenceton University, Prenceton.

Bird, G.A., 1976. Molecular Gas Dynamics. Clarendon Press, Oxford.

Bird, G.A., 1994. Molecular Gas Dynamics and the Direct Simulation of Gas Flows. Oxford Science Publications.

Bird, G.A., 1998. Recent advances and current challenges for DSMC. Computers and Mathematics with Applications 35, 1–14.

Cai, C.P., Boyd, I.D., Fan, J., 2000. Direct simulation method for low-speed microchannel flows. Journal of Thermophysics and Heat Transfer 14, 368–378.

Fang, Y., Liou, W.W., 2002. Computations of the flow and heat transfer in microdevices using DSMC with implicit boundary conditions. Journal of Heat Transfer Transactions of ASME 124, 338–345.

Hadjiconstantinou, N.G., Simek, O., 2002. Constant-wall-temperature Nusselt number in micro and nano-channels. Journal of Heat Transfer 124, 356–364.

Ho, C.M., Tai, Y.C., 1998. Micro-electro-mechanical-systems (MEMS) and fluid flows. Annual Review of Fluid Mechanics 30, 579–612.

Ikegawa, M., Kobayashi, J., 1990. Development of a rarefied flow simulator using the direct-simulation Monte Carlo method. JSME International Journal 30, 463–467.

Lee, S.Y.K., Wong, M., Zohar, Y., 2001a. Pressure losses in microchannels with bends. In: Proceeding IEEE MEMS'01, pp. 491–494.

Lee, W.Y., Wong, M., Zohar, Y., 2001b. Flow separation in constriction microchannels. In: Proceeding IEEE MEMS'01, pp. 495–498.

Li, X., Lee, W.Y., Wong, M., Zohar, Y., 2000. Gas flow in constriction microdevices. Sensors and Actuators A 83, 277–283.

Liou, W.W., Fang, Y.C., 2000. Implicit boundary conditions for direct simulation Monte Carlo method in MEMS flow predictions. Computer Modeling in Engineering and Science 4, 119–128.

Liou, W.W., Fang, Y.C., 2001. Heat transfer in microchannel devices using DSMC. Journal of Microelectromechanical Systems 10, 274–279.

Mohamed, Gad-el-Hak, 1999. The fluid mechanics of microdevices—the Freeman scholar lecture. Journal of Fluids Engineering 121, 5–33.

Nance, R.P., Hash, D.B., Hassan, H.A., 1998. Role of boundary conditions in Monte Carlo simulation of MEMS devices. Journal of Thermophysics and Heat Transfer 12, 447–449.

Oran, E.S., Oh, C.K., Cybyk, B.Z., 1998. Direct simulation Monte Carlo: recent advances and applications. Annual Review of Fluid Mechanics 30, 403–441.

Piekos, E.S., Breuer, K.S., 1996. Numerical modeling of micromechanical devices using the direct simulation Monte Carlo method. Journal of Fluids Engineering 118, 464–469.

Wang, M.R., Li, Z.X., 2002a. Microscale thermal science and its applications in MEMS. Instrument Technique and Sensor 7, 1–4.

Wang, M.R., Li, Z.X., 2002b. Investigation progress in MEMS-based micro fluid machinery. Fluid Machinery 30, 23–28.

Wu, J.-S., Tseng, K.-C., 2001. Analysis of micro-scale gas flows with pressure boundaries using direct simulation Monte Carlo method. Computers and Fluids 30, 711–735.

Wu, J.-S., Lee, F., Wong, S.-C., 2001. Pressure boundary treatment in micromechanical devices using the Derict simulation Monte Carlo method. JSME International Journal 44, 439–450.